Laser-powder bed fusion in-process dispersion of reinforcing ceramic nanoparticles onto powder beds via colloid nebulisation

Andre Mussatto[1, 2, 3, a], Robert Groarke[1, 2, 3], Rajani K. Vijayaraghavan[2, 3, 4], Muhannad Ahmed Obeidi[1, 2, 3], Ronan MacLoughlin[5, 6, 7], Patrick J. McNally[2, 3, 4], Valeria Nicolosi[8, 9, 10] Yan Delaure[1, 2, 3], Dermot Brabazon[1, 2, 3]

[1] School of Mechanical and Manufacturing Engineering, Dublin City University, Glasnevin, Ireland

[2] I-Form Advanced Manufacturing Research Centre, Dublin City University, Glasnevin, Ireland

[3] Advanced Processing Technology Research Centre, Dublin City University, Glasnevin, Ireland

[4] School of Electronic Engineering, Dublin City University, Glasnevin, Ireland

[5] Research and Development, Science and Emerging Technologies, Aerogen Limited, Galway, Ireland

[6] School of Pharmacy and Biomolecular Sciences, Royal College of Surgeons in Ireland, Dublin, Ireland

[7] School of Pharmacy and Pharmaceutical Sciences, Trinity College Dublin, Dublin, Ireland

[8] I-Form Advanced Manufacturing Research Centre, Trinity College Dublin, Dublin, Ireland

[9] Centre for Research on Adaptive Nanostructures and Nanodevices (CRANN) and Advanced Materials and Bioengineering Research (AMBER), Trinity College Dublin, Dublin, Ireland

[10] School of Chemistry, Trinity College Dublin, Dublin, Ireland

[a] Corresponding author: andre.mussatto2@mail.dcu.ie

Abstract

Functionally grading material composition in laser-powder bed fusion grants the potential for manufacturing complex components with tailored properties. The challenge in achieving this is that the current laser-powder bed fusion machine technology is designed to process only powdered feedstock materials. This study presents a multi-feedstock material printing methodology for laser-powder bed fusion. Utilising colloid nebulisation, tungsten carbide nanoparticles were successfully deposited onto powder beds of stainless steel 316L during the laser-powder bed fusion process. By this means, a controlled volume of tungsten carbide nanoparticles was uniformly dispersed onto powder beds under the inert processing chamber atmosphere. As a result, specimens printed with this methodology showed an increase in strength. Similarly, the colloid medium played an important role in the resulting microstructures. It led to the formation of consistent and stable meltpools and a strong crystallographic texture. Recommendations are given for the successful dispersion of higher volumes of nanoparticles. Additionally, insights into application prospects for material nebulisation in laser-powder bed fusion are presented and discussed.

Highlights

- A tungsten carbide colloid was successfully nebulised onto powder beds during the laser-powder bed fusion processing of 316L.

- Colloid nebulisation ensured a uniform dispersion of tungsten carbide within the austenitic microstructure of 316L.

- The 316L specimens were strengthened with tungsten carbide nanoparticles.

Keywords: multi-material powder bed fusion; colloid nebulisation; metal matrix composite; stainless steel 316L; tungsten carbide

1. Introduction

Laser-powder bed fusion (L-PBF) has revolutionised the manufacturing world through its personalised customisation and geometrically intricate capabilities, and through the distinctive resulting microstructures from its rapid cooling and solidification cycles [1]. This reflects on the continuously growing academic research and countless aerospace, automotive and medical industries adopting this technique [2]. Through this revolution a widespread innovation with single-material usage was established [3]. However, the manufacturing world is constantly evolving and today several L-PBF printers have the capability of manufacturing multi-material systems [4].

Multi-material L-PBF enables combining the physical characteristics of different materials into one system to derive a special function that is difficult to achieve through single-material L-PBF or conventional manufacturing methods [5]. Ultimately, multi-material L-PBF can provide solutions to problems associated with fusing dissimilar materials and address inefficiencies in manufacturing by reducing the number of production steps [6,7]. Moreover, multi-material L-PBF entails extensive changes in regard to the design potential by allowing to change the material properties across a single component and thus locally adjust the material to set criteria [8].

Despite Aerosint SA [9] introducing a commercial dual-powder recoating system for L-PBF, the implementation of multi-material processing in L-PBF is still relatively new. Therefore, only limited research exists on this implementation approach in the field of architecture and construction.

The development of multi-material components with sharp and gradient material transitions has been reported in the literature [10–15]. A sharp transition between two dissimilar materials tends to lead to high stress concentration at the interfaces and can even cause delamination under complex loading conditions [16]. Nevertheless, this can be suppressed by a smooth material gradient transition or remediated by heat treatment [17]. A disadvantage of this multi-material approach is that it provides difficulties with controlling contamination between each powder [18]. Still, several multi-material system such as 316L/CuSn10 [19], IN718/GRCop-42 [20] and AlSi10Mg/C18400 [21] have been successfully developed.

Multi-material L-PBF processing of a feedstock mixture composed of two or more materials typically requires an additional process to blend the powders together [22]. Similar to the in-situ powder deposition [23], the major challenge with this is to ensure that the mixture is homogeneous within a layer and consistent between layers [24,25]. As an alternative, feedstocks of atomised powder blends [26,27] or coated powders [28,29] could be used at the expense of additional processing steps and cost. The capability of L-PBF to process powder mixtures has created exciting material research opportunities in the field of composites [30]. Derived from this, L-PBF of powder mixtures has also been explored for alloy development applications [15]. This in-situ alloying strategy has shown a potential for rapid design and verification of new alloys.

As can be seen from the current state of art, multi-material L-PBF has opened up a broad spectrum of possibilities for more complexity and functionality to new applications. At present, L-PBF systems and its research are restricted to powdered feedstocks. Therefore, the form of feedstock barrier needs to be overcome in order to achieve further advancements in multi-material L-PBF. To address this issue, this work introduces a method for laser-powder bed fusing multiple forms of feedstock materials. In summary, a colloid feedstock of tungsten carbide (WC) is nebulised onto powder beds of 316L during the laser-powder bed fusion process. To assess this methodology, the printed specimens are characterised at microstructural level and contrasted with traditionally printed specimens. Discussions are then launched to illustrate the research advancements coming from this methodology. Additionally, insights into application prospects for material nebulisation in laser-powder bed fusion are presented.
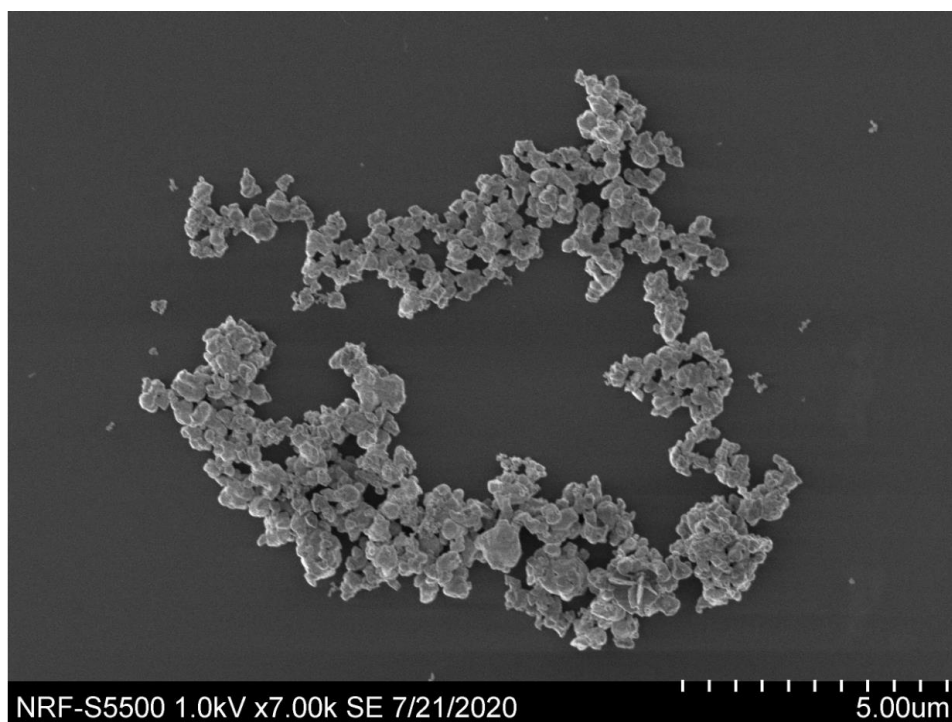
2. Experimental

2.1 Materials and Methods

Vacuum melted argon gas atomised stainless steel AISI 316L powder (35-50 µm) supplied by Mimete S.r.l. and nanometre sized (30-100 nm) hexagonal WC powder supplied by US Research Nanomaterials Inc. were used in this study. The morphology of these powders is shown in Figure 1.
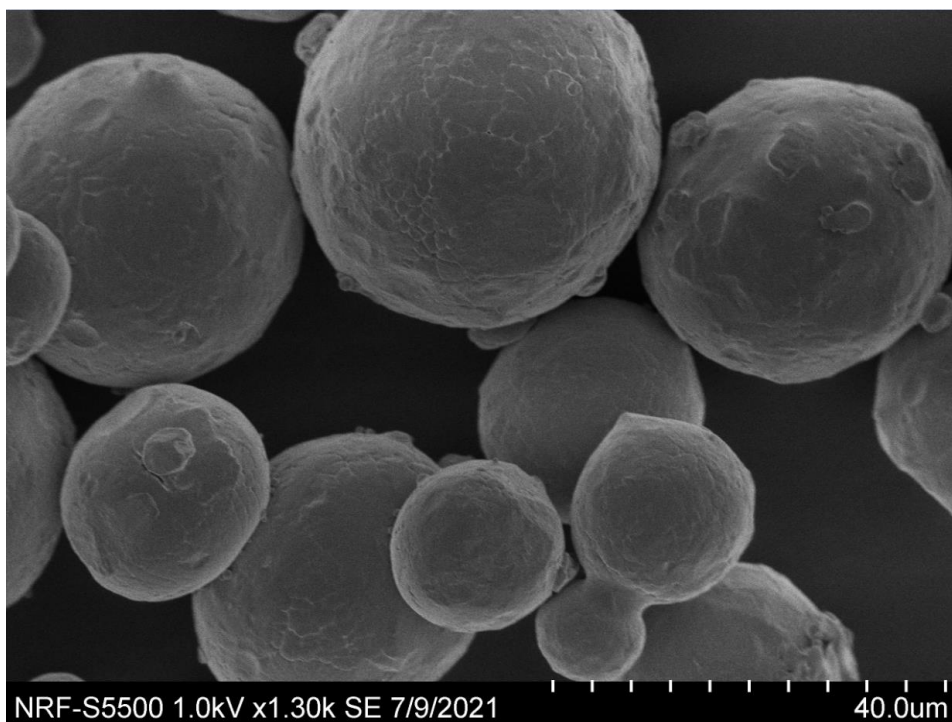
(a)

(b)

Figure 1 Scanning electron micrographs of (a) 316L and (b) WC powder.

A colloid consisting of WC 2wt. % in deionised water was prepared. Then, a homogeneous nanoparticle dispersion was obtained using an in-house developed system based on the THINKY PR-1 mixer. The dynamic viscosity of the prepared colloid (vial labelled WC2 in Figure 2) was determined on an Anton Paar MCR 301 rotational

rheometer equipped with a stainless steel cone plate (CP50-2, Anton Paar) of 50 mm in diameter and 2° angle. The plate gap was set to 208 µm and the temperature was controlled at 20±0.1 °C using a Peltier element during the measurement.
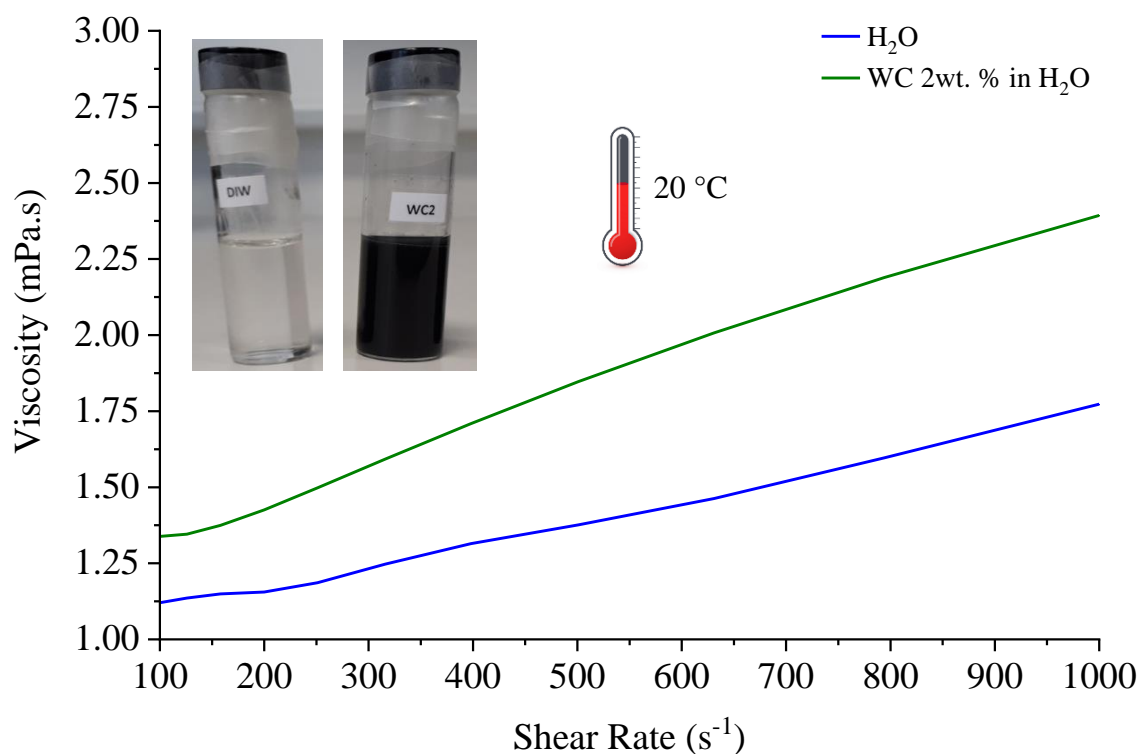
**Figure 2** Rheological performance of the colloidal system prepared in this study.

The deposition of this colloid onto powder beds during the printing process was achieved using a vibrating mesh Aerogen© Pro nebuliser. The aerosol jet was projected onto a circular area of 50 mm diameter of the powder bed. Approximately, 0.5 ml of the prepared WC colloid was deposited in each of the 20 powder bed layers. The evaporation of deposited colloid droplets on the powder was approximately 20 seconds. Video 1 in the Appendix shows the evaporation time lapse of nebulised deionised water droplets. During printing, the evaporated water was automatically vented out from the printer's processing chamber by the constant 2 l/min argon flow, and any remaining evaporation/condensation was then extracted by the argon circulation/filtration system at its active stages.

4x4x4 mm^3 cuboids were printed using an Aconity Mini (Aconity GmbH, Germany) as per coordinates shown in Figure 3. The prints were repeated three times for the 316L and WC-316L builds. All prints were performed in an argon atmosphere with the oxygen level kept below 100 ppm. The laser power, scanning speed, layer thickness, laser spot diameter, hatch distance and hatch translation per layer were set as 160 W, 600 mm/s, 50 µm, 50 µm, 40 µm and 20 µm, respectively. The scanning strategy was based on the unidirectional stripe hatching system. In summary, layer printing cycles consisted of: powder spreading, nanoparticle nebulisation onto powder bed and powder bed selective lasing. This process is illustrated in Figure 4 and is shown in Video 2 of the Appendix.
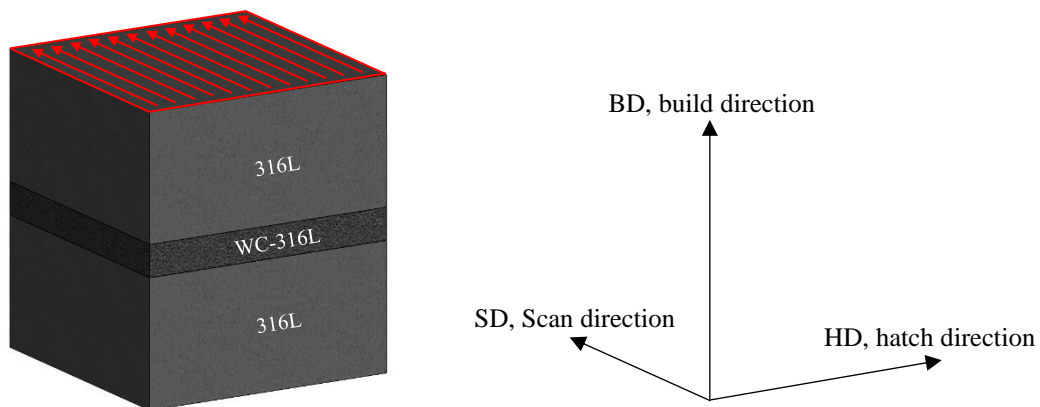
Figure 3 Coordinates and laser scanning strategy of the 4x4x4 mm^3 cuboid printed specimens.
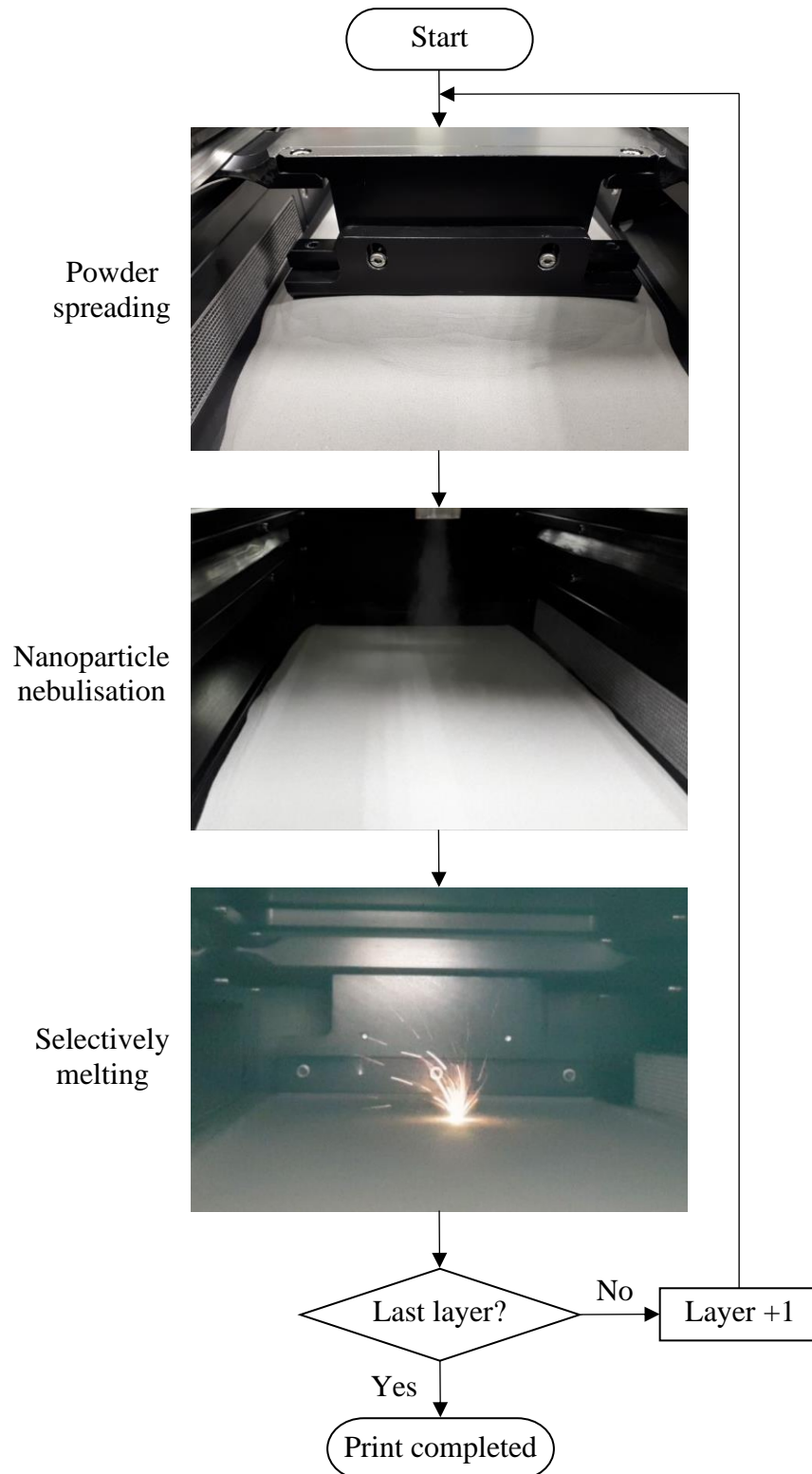
Figure 4 Illustration of the layer printing cycle employed for the manufacturing of WC-316L specimens.

2.2 Characterisation

The density of the printed specimens was measured with a Micromeritics AccuPyc 1330 helium pycnometer. The mechanical properties were measured via nano indentation using a Bruker Hysitron TI Premier USA equipped with a standard Berkovich diamond indenter. An array of 10x3 indentations was performed with 10 mN load and intervals of 30 µm. The chemical composition of the specimens was investigated using an energy dispersive x-ray detector coupled into a Hitachi S5500 field emission scanning electron microscope. A JEOL JSM-IT100 scanning electron microscope was used to obtain microstructural images. Phase constituents and crystallographic texture of the specimen were investigated using a triple-axis Jordan Valley Bede D1 high resolution x-ray diffraction system with a copper ($\lambda = 1.5405$ Å) radiation source operated at 45 kV and 40 mA, and a Zeiss Supra 40 field emission scanning electron microscope equipped with a Bruker e-FlashHR electron backscatter diffraction detector. The above characterisations were performed in the plane of the specimens normal to the hatching direction.

3. Results and Discussion

3.1 Microstructure

The scanning electron micrographs in Figure 5 contrast the microstructure of the specimens. It is worth noting that the resultant solidified microstructures are very similar. The solidification structure is that of columnar grains containing colonies of submicrometric cells separated by low angle grain boundaries. These columnar grains arose due to partial remelting of the previous consolidated layers, as they allowed epitaxial growth. Therefore, this epitaxial growth from the parent grains encouraged the elongation of the columnar grains, which then resulted in a highly textured columnar microstructure, as confirmed later by the electron backscatter diffraction analysis. From the shown plane of view, microstructural features of periodically layer bands are common in L-PBF specimens [31–36]. Accordingly, the behaviour of the layer bands observed in Figure 5 resulted from reheat and remelt influence by the consecutive layer deposition. In summary, these layer bands were weak barriers to prevent columnar grain size growth. However, as observed from the high magnification inset micrographs in Figure 5, layer bands did effectively break the cellular structures into small colonies. Consequently, neighbouring colonies of cells grew rather misoriented to each other in response to the influence of the layer bands to the local maximum heat flux direction. Therefore, this randomised orientation of the colonies contrasted with the columnar grains anisotropy. The benefit of this is that such subgrain features could result in strengthening and toughening effects by impeding dislocation movement and altering the course of fracture and propagation paths.
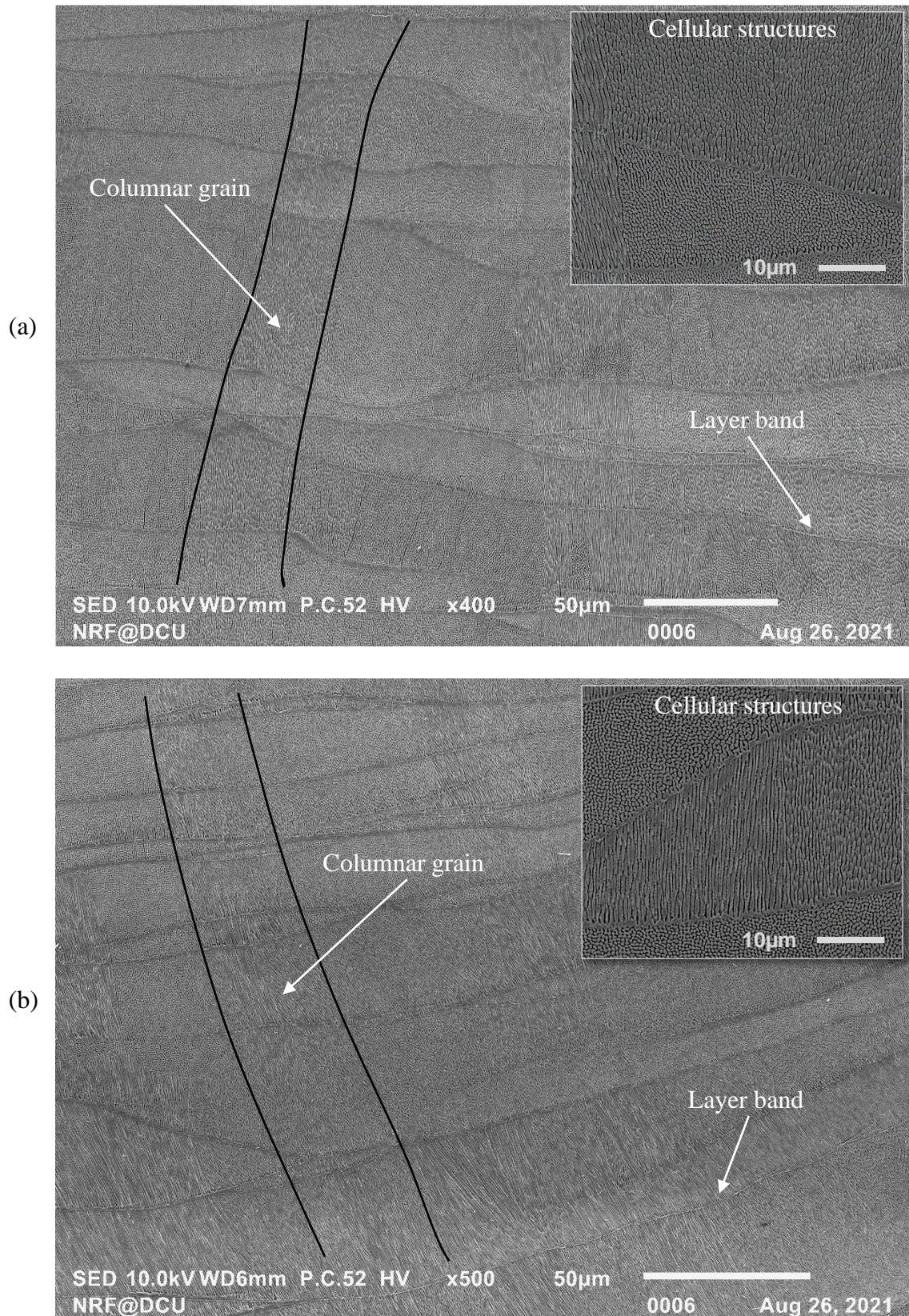
Figure 5 Microstructure viewed from the plane normal to the hatching direction of (a) 316L and (b) WC-316L.

3.2 Density

The densities of the printed specimens obtained via helium pycnometry are shown in Table 1. Based on the true density of 316L, 7.98 g/cm^3 [37], it can be concluded that near fully dense specimens were printed in this study. During the printing of the WC-316L specimen, in response to the nebulised material, it is possible that some of the evaporated water molecules got trapped in the molten pools causing hydrogen porosity in the solidified microstructure. However, the difference in density between the specimens was very small, hence this effect could be neglected. Additionally, Figure 5 shows no evidence of microstructural porosity or lack of fusion defects in the specimens, and this observation is consistent with the density results of Table 1. Therefore, the experimental conditions and input processing parameters used were suitable for printing dense specimens. Such high density values are desired in order to be more effective in improving the properties of materials. Therefore, the printing of a near fully dense WC-316L specimen could enable a significant increase in strength while maintaining the good ductility of the matrix 316L alloy.

Table 1 Density measurement results, n=10.

Specimen	Density (g/cm^3)
316L	7.95±0.024
WC-316L	7.92±0.021

3.3 Nano Hardness

The mechanical behaviour of the printed specimens was characterised by nano indentation with a maximum load of 10 mN, in the plane normal to the hatching direction. The load-depth curves of Figure 6 shows that the nebulised WC colloid strengthened the 316L matrix, as observed from the reduced indentation depth and steeper unloading slope. This can be ascribed to the existence of a brittle and mechanically hard intermetallic phase. The nano indentation hardness and modulus measurements are presented in Table 2. Typically, the nano hardness of L-PBF 316L is about 3 GPa [38–40]. Therefore, the obtained 3.21 GPa is in relatively good agreement with the literature. The variation in hardness may be attributed to the processing conditions, resultant residuals stress, grain size and crystallographic texture promotion of high dislocation density and formation of a dense network of slip bands. The difference in hardness between the specimens indicates different elastic-plastic deformation characteristics. Therefore, according to the measured hardnesses, the WC-316L specimen produced less plastic deformation during the nano indentation testing. This was because the hard WC nanoparticles limited localised plastic deformation. The reduced modulus correlated with the hardness, showing an increase of nearly 12 GPa in the WC-316L specimen, which can be related to the stiffening effect introduced by the WC nanoparticles. In summary, one should note that the overall mechanical improvements were very small. Nevertheless, they do correlate well with the amount of nebulised WC.
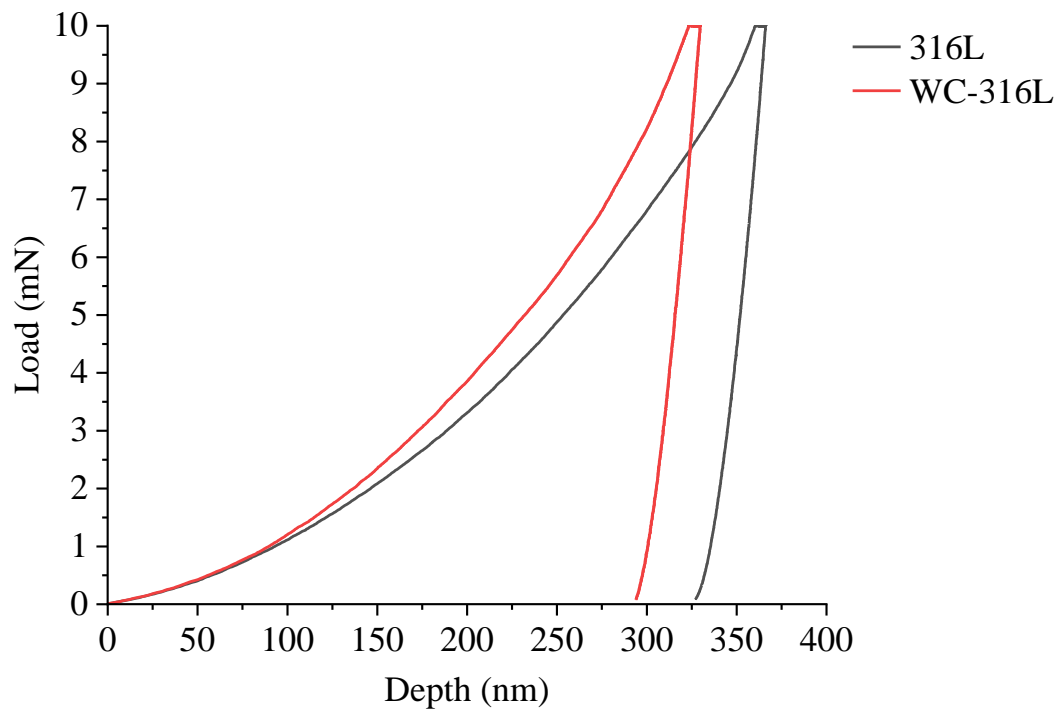
Figure 6 Nano indentation load-depth curve of the 316L and WC316L specimen.

Table 2 Nano indentation hardness and reduced modulus of the specimens; n=30.

Specimen	Nano Hardness (GPa)	Reduced Modulus (GPa)
316L	$3.21_{\pm0.12}$	$195.37_{\pm2.98}$
WC-316L	$3.51_{\pm0.08}$	$207.20_{\pm5.27}$

3.4 Chemical analysis

The results of the elemental analysis performed on the printed specimens are shown in Figure 7 and Table 3. Unfortunately, Figure 7(a) and Table 3 reveal tungsten contamination in the 316L composition. After investigations, it was concluded that the supplied powder was contaminated possibly during its atomisation. However, the amount of contamination was small and the elemental composition of the 316L is now known, therefore it can be contrasted with the elemental composition of the WC-316L specimen. Figure 7(b) shows the contribution of the nebulised colloid to the elemental composition of 316L. It is worth noting the increased distribution of tungsten within the analysed area of the WC-316L specimen, which also verifies that a uniform dispersion of WC was achieved via nebulisation. A shortcoming of many conventional manufacturing processes is the high tendency of reinforcing nanoparticles for agglomeration and clustering and the challenge in achieving a uniform dispersion of reinforcement in metal matrix composites [41,42]. Therefore, in-situ nebulisation of reinforcing nanoparticles within the L-PBF process proved to be an alternative solution to these problems.
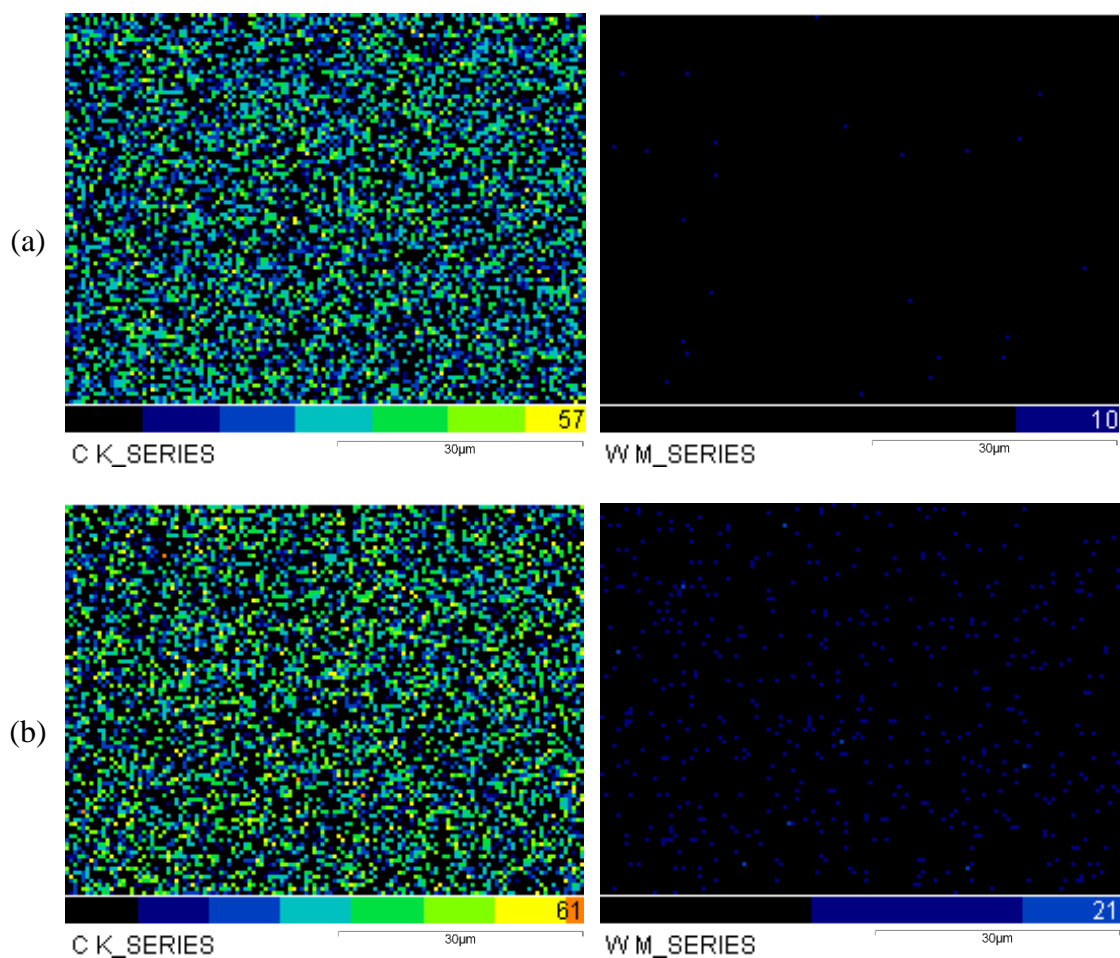
Figure 7 Chemical composition of the specimens with mapping of carbon and tungsten for (a) 316L and (b) WC-316L.

**Table 3** Quantified chemical composition of the specimens.

Element	316L	WC-316L
C (wt. %)	5.5	5.59
W (wt. %)	0.22	0.38
Fe (wt. %)	64.75	63.05
Cr (wt. %)	15.85	16.73
Ni (wt. %)	10.66	11.18
Mo (wt. %)	2.06	1.96
Mn (wt. %)	0.96	1.11

3.5 Crystallography

3.5.1 Phase

Constituent phase identification using X-ray diffraction revealed an intricate multiphase mixture in the specimens, see Figure 8. Conventionally and additively processed austenitic stainless steels are very often reported as being influenced by precipitation reactions [22,43,44]. The formation of austenite in 316L depends on cooling rate and

chemical composition, and if the Cr/Ni ratio is low then the possibility of iron-silicon precipitation is suppressed [45]. The precipitated hard Fe_2Si phase plays a crucial role in determining the material response. However, while improving hardness and wear, corrosion, fatigue and fracture resistance of the specimens could be compromised by the brittle intermetallic Fe_2Si precipitates [46–48]. An evident diffraction peak of SiC was observed in the specimens' spectrum and confirmed by the JCPDS card 89-1396. It is therefore clear that the energy applied to fuse the 316L powder also triggered an exothermic chemical reaction which produced new chemical compounds and also possibly generated enough thermal energy for the propagation of more chemical reactions. Therefore, it is most likely that the formation of SiC was achieved via a solution-precipitation mechanism from the silicon and carbon atoms in the 316L melt. In-situ formed reinforcements are thermodynamically stable at the matrix, leading to less degradation in elevated temperature applications. Additionally, the grains are finer in size and their distribution in the matrix is more uniform yielding better mechanical properties and the matrix-reinforcement interfaces are clean, resulting in a strong interfacial bonding [7]. The existence of WC was confirmed in both specimens, hence it could be concluded that the tungsten contamination in the 316L powder reacted with carbon during the L-PBF process and formed WC precipitates. Also, there is no evidence that the nebulised WC colloid dissolved and formed other tungsten compounds with the matrix elements. Therefore, the x-ray diffraction analysis revealed Fe_2Si, SiC and WC reinforcing phases in the specimens. Then the electron backscatter diffraction analysis indicated that discrepancies in mechanical properties between specimens resulted from the nebulised tungsten carbide nanoparticles and an increased fraction of the precipitated silicon carbide phase in the WC-316L specimen, see Table 4.
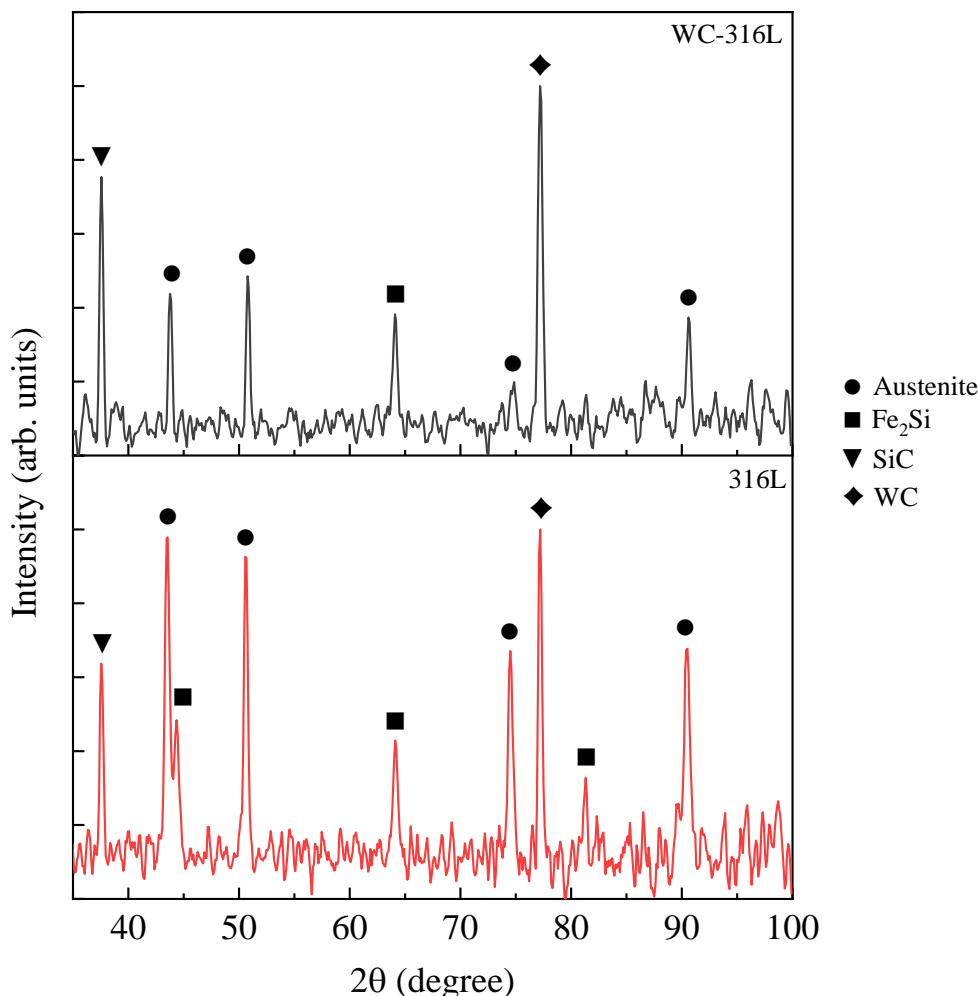
Figure 8 X-ray diffraction patterns of the printed specimens.

Table 4 Electron backscatter diffraction estimated phase distribution for the 316L and WC-316L specimen.

Phase	Phase Distribution (%)	
	316L	**WC-316L**
Austenite	98.81	98.51
Fe$_2$Si	0.75	0.66
SiC	0.01	0.03
WC	0.12	0.23
Zero Solution	0.31	0.57

3.5.2 Texture

Representative electron backscatter diffraction orientation map, pole figure and inverse pole figure of the 316L and WC-316L specimens are shown in Figure 9. Large irregular columnar grains going through several powder layers are visible, which indicate that the solidification occurred by epitaxial growth. The 316L specimen exhibited a rotated {100} cube texture component with a combination of <001> and <101> orientation aligned nearly parallel to the build and scan directions. This may be visualised in the grain map

of Figure 9a where most of the grains appear to be inclined about -30° with respect to the build direction. In contrast, it was confirmed the development of a strong {100} <001> cube texture in the WC-316L specimen. In fact, it is worth noting the high intensity in <001> in the respective inverse pole figure which reflects on the observed grains in Figure 9b. Therefore, in this regard, the growth of highly oriented columnar grain structures in the build direction corresponded to the existence of a highly uniform maximum temperature gradient within the meltpools of the specimen WC-316L.
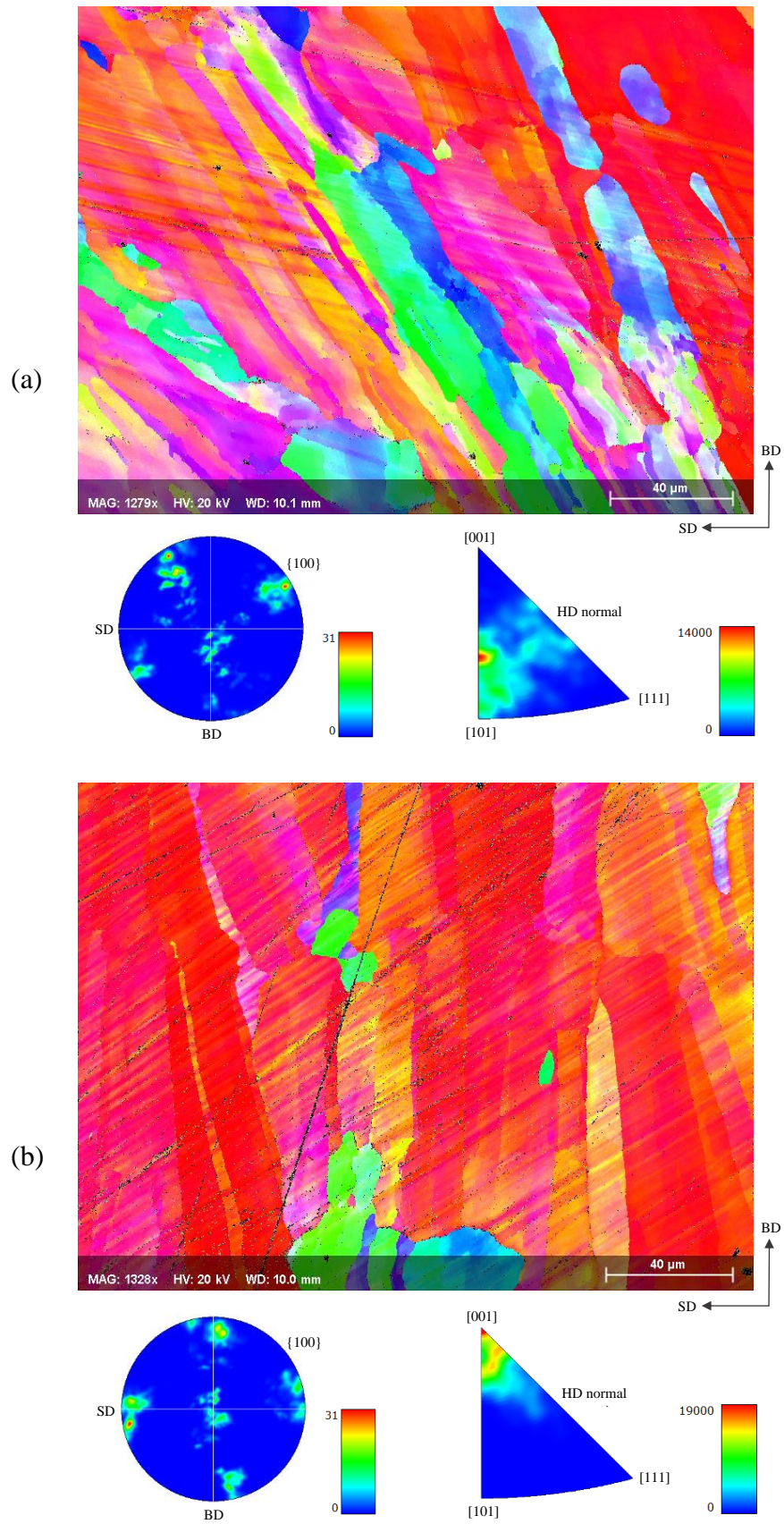
Figure 9 Grain map and texture of (a) 316L and (b) WC-316L.

To understand the reasons for the observed discrepancies in the crystallographic textures, single track scanning experiments were carried out. Figure 10 contrasts the effect of colloid nebulisation on single track formation. During the printing of the WC-316L specimens, it is possible that the native porosity within the 316L powder beds trapped colloid droplets preventing the full evaporation of the colloid medium (deionised water). Therefore, residual water molecules could have interacted with the laser beam and also ended up being mixed with the molten metal, and consequently altered the meltpool cross-sectional profile in relation to those of the 316L specimens. The literature suggests that increasing the laser input energy and or the efficiency of the photonic absorption by the irradiated material reduces the meltpool contact angle and increases the depth and width of solidified tracks [49–51]. It is also known that residual water molecules and water vapour can cause radiation attenuation of the laser beam [52–54]. Additionally, the upward speed of the ejected plume flux is intensified as water vapour is merged with the existing metal vapour. This then introduces a low pressure zone near the melpool and thereupon the Bernoulli effect-driven gas flow. Consequently, several powder particles from the powder bed are entrained in the convective gas flow and draw into and become consolidated with the meltpool [55,56]. Therefore, it was concluded that the shallowing of the meltpool shown in Figure 10b was due to the laser beam intensity attenuation resulting from residual water molecules, and the seen larger width was due to the addition of material consolidation to the meltpool. In agreement with the presented study, it was reported elsewhere that shallow and wide meltpools promote the formation of <001> texture [57]. Additionally, both of the tracks showed normal meltpool geometries dominated by a conductive mode of heat transfer [58]. In this regard, the conductive mode characterised stable meltpools with low depth to width ratios which resulted in minimal porosity defects in the microstructure of the specimens.
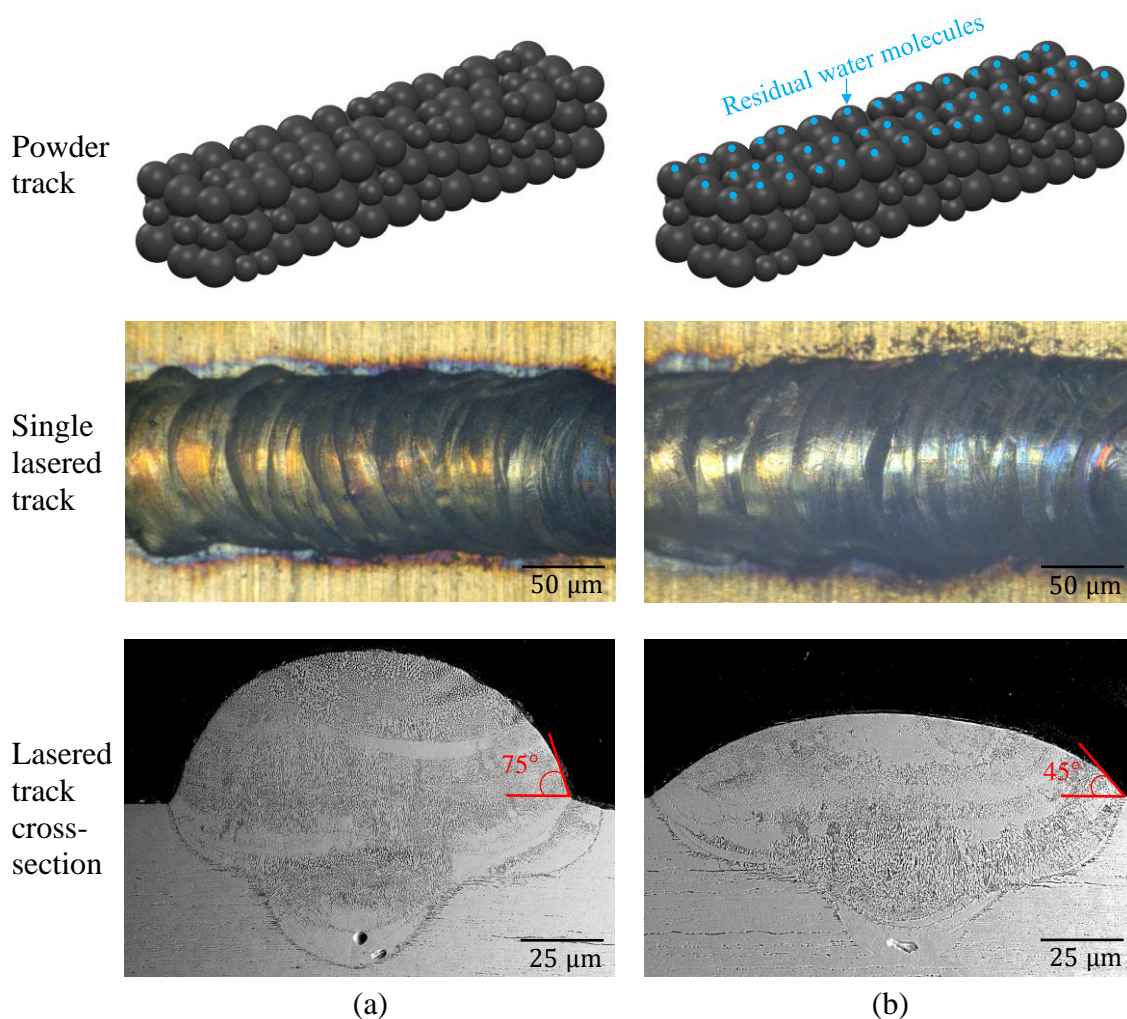
Figure 10 Cross-section of single tracks formed (a) without and (b) with colloid nebulisation.

4. Discussion

4.1 Current Achievements

This study successfully deposited colloidal feedstock of WC onto powder beds during the laser-powder bed fusion of 316L. The results presented in the previous section demonstrated that the incorporation of material nebulisation to laser-powder bed fusion is a promising method for tailoring and improving the properties of printed specimens. Additionally, this new method has shown a clear potential for the development of metal matrix composites within a single step production process.

Here, all the specimens presented a nearly full dense microstructure with values close to the true density of 316L. The higher hardness and modulus of the WC-316L specimen resulted from the Orowan strengthening mechanism. In this regard, the presence of the reinforcing particles promoted deformation resistance by preventing dislocation motion and propagation. The difference in meltpool shapes was the origin for developing different crystallographic textures. In response to its shallowed and widened meltpools, grains in the WC-316L specimen grew highly parallel to the build direction and the resulting texture was then strong in the <001> direction. Therefore, as the formation of a

strong texture is an effective way of improving strength [59], the mechanical improvements found were ascribed to the presence of the reinforcing particles and the resultant crystallographic texture.

4.2 Methodological Limitations

One of the limitations of using the nebulisation route was its low volume nanoparticle deposition capability. The 2wt. % colloid concentration employed was the highest concentration capable of maintaining a stable and high throughput rate of droplets. Colloids prepared with higher concentrations were observed to be unstable on account of nanoparticle aggregation and sedimentation. Additionally, the use of stabilisers was found unfeasible for the given application as these altered the viscosity of the colloid, which the nebuliser was sensitive to. Also, it was found that the nebulisation of a higher volume of colloid per layer than that used in this study would inhibit the formation of quality powder beds, see Figure 11. This was because the powder bed became saturated with the colloid medium and hence increased the cohesive and adhesive forces between particles. Then, as a result, the forming of the consecutive powder bed layer removed patches of powder from the previous powder bed layer. It is also worth noting that the quality of the powder bed near the consolidated powder was unaffected. Since this area is at higher temperature, a more efficient evaporation of the colloid medium was here achieved. Based on the aforementioned limitations and challenges, future work should use stable and highly concentrated colloids (> 5 wt. %) synthesised from low density ceramics such as silicon carbide, boron carbide, aluminium oxide and titanium carbide. Additionally, it is recommended the use of a printer which is equipped with a counter-rotating roller spreading system as the compaction of powder could in this case result in higher powder bed qualities [60].
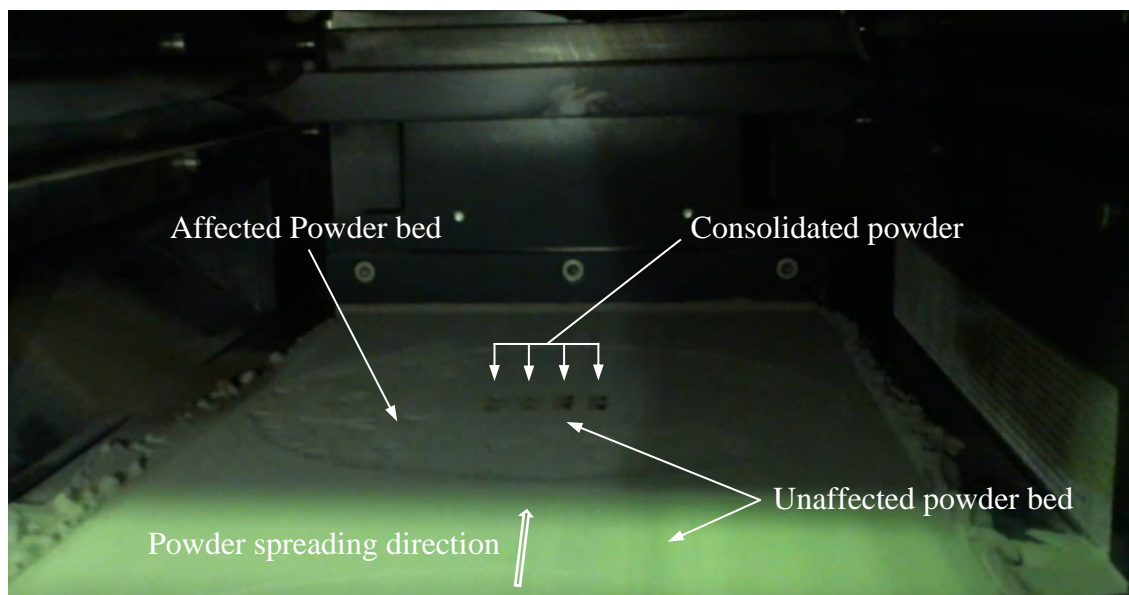
Figure 11 Picture of the detrimental effect on the powder bed when an excessive volume of colloid is deposited per layer.

4.3 Application Prospects of Material Nebulisation in Laser-Powder Bed Fusion

To date only powdered forms of feedstock materials have been used within the laser-powder bed fusion process. In order to open a window for the development of new technological materials, the nebulisation of colloid feedstock onto powder beds emerged as a potential solution for improving and tailoring the properties of laser-powder bed fused components. The presented multi-feedstock material printing methodology proved to be capable of uniformly dispensing nanoparticles onto powder beds and controlling crystallographic texture. This methodology also showed a unique approach to metal matrix composite fabrication which advantages should be further explored.

The following are examples of what else material nebulisation in laser-powder bed fusion could be used for.

(1) The nebulisation of deionised water could be used for the nucleation and growth of hydrogen gas bubbles which then can be trapped by the process solidification front [61]. This could be particularly useful for printing functional graded porous structures such as for orthopaedic implants.

(2) Grain fining agents such as colloids of $Fe_{0.35}C_{0.15}Ti_{0.25}Nb_{0.25}$ could be nebulised onto metallic powder beds during the laser-powder bed fusion process [62–64]. As there is a growing demand for materials with strengths greater than those found in currently available alloys [65,66], the aforementioned should be considered.

(3) Colloids such as those of graphene, silver and copper could be nebulised onto powder beds to increase the electrical and thermal conductivity of laser-powder bed fused components [67–70]. With the recent electric vehicle revolution, this could be advantageous towards improving the current efficiency of electric vehicles.

(4) When laser-powder bed fusing dissimilar materials for example metals and ceramics where wetting may be an issue or when the melting temperature needs to be lowered in order to preserve the processing material properties, then a colloid intermediary bonding layer containing for example aluminium, copper, silver, nickel or tin compounds could be nebulised onto the powder beds [71–74].

(5) Silver, copper and aluminium are the most challenging materials for laser-powder bed fusion due to their low optical absorption in the near infrared [75,76]. Based on the literature, the nebulisation of carbon and iron colloids could be used to increase the interactions between the laser beam and powder bed particles [77–80].

(6) Laser-powder bed fusion has also recently been considered for repairing high value components such as damaged or worn gas turbine blades and high performance tools [81–84]. However, the strength at the repaired zone depends on the interfacial integrity between the component and the new added material. Therefore, in-situ nebulisation of flux to dissolve oxides from the surface to be repaired and the nebulisation of chemical compounds to purify meltpools should be implemented in the laser-powder bed fusion repair applications [85,86].

4. Conclusions

This article presents a multi-feedstock material printing methodology for the established laser-powder bed fusion manufacturing technique. In summary, tungsten carbide nanoparticles were uniformly dispersed onto powder beds of stainless steel 316L via colloids nebulisation during the laser-powder bed fusion process.

Nearly full dense microstructures with values close to the true density of 316L were obtained. The nebulised tungsten carbide nanoparticles strengthened the 316L matrix which increased the nano hardness and modulus of the specimens. Overall, the achieved mechanical improvements were small, but they do correspond with the small amount of nebulised tungsten carbide colloid.

Surprisingly, the colloid medium promoted positive effects on the resulting microstructures. This was evidenced by the stable meltpools which were dominated by the conductive mode of heat transfer. The consistent low depth to width ratio of the meltpools played an important role in the resulting microstructure. The most interesting fact was that it led to the growth of grains highly parallel to the build direction and so the resulting texture was very strong in the <001> direction.

To conclude, this study proved that it is feasible to deposit nanoparticles onto powder beds via colloid nebulisation. Additionally, this methodology showed a clear potential for the development of metal matrix composites with a single step production process. Other possible applications of material nebulisation in laser-powder bed fusion together with recommendations can be found within this article.

Acknowledgments

Appendix

Video 1 Evaporation time lapse of nebulised water droplets.

Video 2 Laser-powder bed fusion in-process dispersion of ceramic nanoparticles onto powder beds via colloid nebulisation.

References

[1] Salman, O. O., Gammer, C., Chaubey, A. K., Eckert, J., and Scudino, S., 2019, "Effect of Heat Treatment on Microstructure and Mechanical Properties of 316L Steel Synthesized by Selective Laser Melting," Mater. Sci. Eng. A, **748**, pp. 205–212.

[2] Yap, C. Y., Chua, C. K., Dong, Z. L., Liu, Z. H., Zhang, D. Q., Loh, L. E., and Sing, S. L., 2015, "Review of Selective Laser Melting: Materials and Applications," Appl. Phys. Rev., **2**(4).

[3] Wei, C., Li, L., Zhang, X., and Chueh, Y.-H., 2018, "3D Printing of Multiple Metallic Materials via Modified Selective Laser Melting," CIRP Ann., **67**(1), pp. 245–248.

[4] Gu, H., Wei, C., Li, L., Han, Q., Setchi, R., Ryan, M., and Li, Q., 2020, "Multi-Physics Modelling of Molten Pool Development and Track Formation in Multi-Track, Multi-Layer and Multi-Material Selective Laser Melting," Int. J. Heat Mass Transf., **151**, p. 119458.

[5] Veron, F., Lanoue, F., Baco-Carles, V., Kiryukhina, K., Vendier, O., and Tailhades, P., 2020, "Selective Laser Powder Bed Fusion for Manufacturing of 3D Metal-Ceramic Multi-Materials Assemblies," Addit. Manuf., **50**.

[6] Tan, C., Zhou, K., Ma, W., and Min, L., 2018, "Interfacial Characteristic and Mechanical Performance of Maraging Steel-Copper Functional Bimetal Produced by Selective Laser Melting Based Hybrid Manufacture," Mater. Des., **155**, pp. 77–85.

[7] Mussatto, A., Ahad, I. U., Mousavian, R. T., Delaure, Y., and Brabazon, D., 2021, "Advanced Production Routes for Metal Matrix Composites," Eng. Rep., **3**(5).

[8] Wiscombe, T., 2012, "Beyond Assemblies: System Convergence and Multi-Materiality," Bioinspir. Biomim., **7**(1).

[9] Neirinck, B., Li, X., and Hick, M., 2021, "Powder Deposition Systems Used in Powder Bed-Based Multimetal Additive Manufacturing," Acc. Mater. Res., **2**(6), pp. 387–393.

[10] Wang, H., Chen, J., Luo, H., Wang, D., Song, C., Yao, X., Chen, P., and Yan, M., 2022, "Bimetal Printing of High Entropy Alloy/Metallic Glass by Laser Powder Bed Fusion Additive Manufacturing," Intermetallics, **141**.

[11] Koopmann, J., Voigt, J., and Niendorf, T., 2019, "Additive Manufacturing of a Steel–Ceramic Multi-Material by Selective Laser Melting," Metall. Mater. Trans. B, **50**(2), pp. 1042–1051.

[12] Chen, J., Yang, Y., Song, C., Zhang, M., Wu, S., and Wang, D., 2019, "Interfacial Microstructure and Mechanical Properties of 316L /CuSn10 Multi-Material Bimetallic Structure Fabricated by Selective Laser Melting," Mater. Sci. Eng. A, **752**, pp. 75–85.

[13] Tan, C., Wang, D., Ma, W., and Zhou, K., 2021, "Ultra-Strong Bond Interface in Additively Manufactured Iron-Based Multi-Materials," Mater. Sci. Eng. A, **802**.

[14] Zhang, X., Wei, C., Chueh, Y.-H., and Li, L., 2018, "An Integrated Dual Ultrasonic Selective Powder Dispensing Platform for Three-Dimensional Printing of Multiple Material Metal/Glass Objects in Selective Laser Melting," J. Manuf. Sci. Eng., **141**(1).

[15] Sing, S. L., Huang, S., Goh, G. D., Goh, G. L., Tey, C. F., Tan, J. H. K., and Yeong, W. Y., 2021, "Emerging Metallic Systems for Additive Manufacturing: In-Situ Alloying and Multi-Metal Processing in Laser Powder Bed Fusion," Prog. Mater. Sci., **119**.

[16] Mahamood, R. M., and Akinlabi, E. T., 2015, "Laser Metal Deposition of Functionally Graded Ti6Al4V/TiC," Mater. Des., **84**, pp. 402–410.

[17]   Li, Y., Feng, Z., Hao, L., Huang, L., Xin, C., Wang, Y., Bilotti, E., Essa, K., Zhang, H., Li, Z., Yan, F., and Peijs, T., 2020, "A Review on Functionally Graded Materials and Structures via Additive Manufacturing: From Multi-Scale Design to Versatile Functional Properties," Adv. Mater. Technol., **5**(6).

[18]   Wei, C., and Li, L., 2021, "Recent Progress and Scientific Challenges in Multi-Material Additive Manufacturing via Laser-Based Powder Bed Fusion," Virtual Phys. Prototyp., **16**(3), pp. 347–371.

[19]   Chen, K., Wang, C., Hong, Q., Wen, S., Zhou, Y., Yan, C., and Shi, Y., 2020, "Selective Laser Melting 316L/CuSn10 Multi-Materials: Processing Optimization, Interfacial Characterization and Mechanical Property," J. Mater. Process. Technol., **283**.

[20]   Walker, J., Middendorf, J. R., Lesko, C. C. C., and Gockel, J., 2021, "Multi-Material Laser Powder Bed Fusion Additive Manufacturing in 3-Dimensions," Manuf. Lett.

[21]   Sing, S. L., Lam, L. P., Zhang, D. Q., Liu, Z. H., and Chua, C. K., 2015, "Interfacial Characterization of SLM Parts in Multi-Material Processing: Intermetallic Phase Formation between AlSi10Mg and C18400 Copper Alloy," Mater. Charact., **107**, pp. 220–227.

[22]   Mussatto, A., Groarke, R., A-Hameed, A., Ahad, I. U. I., Vijayaraghavan, R. K., O'Neill, A., McNally, P., Delaure, Y., and Brabazon, D., 2019, "Evaluation via Powder Metallurgy of Nano-Reinforced Iron Powders Developed for Selective Laser Melting Applications," Mater. Des., **182**.

[23]   Wei, C., Sun, Z., Chen, Q., Liu, Z., and Li, L., 2019, "Additive Manufacturing of Horizontal and 3D Functionally Graded 316L/Cu10Sn Components via Multiple Material Selective Laser Melting," J. Manuf. Sci. Eng., **141**(8).

[24]   Diener, S., Zocca, A., and Günster, J., 2021, "Literature Review: Methods for Achieving High Powder Bed Densities in Ceramic Powder Bed Based Additive Manufacturing," Open Ceram., **8**.

[25]   Mussatto, A., Groarke, R., O'Neill, A., Obeidi, M. A., Delaure, Y., and Brabazon, D., 2021, "Influences of Powder Morphology and Spreading Parameters on the Powder Bed Topography Uniformity in Powder Bed Fusion Metal Additive Manufacturing," Addit. Manuf., **38**.

[26]   Mair, P., Kaserer, L., Braun, J., Weinberger, N., Letofsky-Papst, I., and Leichtfried, G., 2021, "Microstructure and Mechanical Properties of a TiB2-Modified Al–Cu Alloy Processed by Laser Powder-Bed Fusion," Mater. Sci. Eng. A, **799**.

[27]   Chen, M., Li, X., Ji, G., Wu, Y., Chen, Z., Baekelant, W., Vanmeensel, K., Wang, H., and Kruth, J.-P., 2017, "Novel Composite Powders with Uniform TiB2 Nano-Particle Distribution for 3D Printing," Appl. Sci., **7**(3), p. 250.

[28]   Zhang, C., Wang, R., Cai, Z., Peng, C., Feng, Y., and Zhang, L., 2015, "Effects of Dual-Layer Coatings on Microstructure and Thermal Conductivity of Diamond/Cu Composites Prepared by Vacuum Hot Pressing," Surf. Coat. Technol., **277**, pp. 299–307.

[29]   Wang, S., Zhu, S., Cheng, J., Qiao, Z., Yang, J., and Liu, W., 2017, "Microstructural, Mechanical and Tribological Properties of Al Matrix Composites Reinforced with Cu Coated Ti3AlC2," J. Alloys Compd., **690**, pp. 612–620.

[30]   Kruth, J.-P., Levy, G., Klocke, F., and Childs, T. H. C., 2007, "Consolidation Phenomena in Laser and Powder-Bed Based Layered Manufacturing," CIRP Ann., **56**(2), pp. 730–759.

[31]   Nadammal, N., Mishurova, T., Fritsch, T., Serrano-Munoz, I., Kromm, A., Haberland, C., Portella, P. D., and Bruno, G., 2021, "Critical Role of Scan Strategies on the Development of Microstructure, Texture, and Residual Stresses during Laser Powder Bed Fusion Additive Manufacturing," Addit. Manuf., **38**.

[32]   Wan, H. Y., Zhou, Z. J., Li, C. P., Chen, G. F., and Zhang, G. P., 2018, "Effect of Scanning Strategy on Grain Structure and Crystallographic Texture of Inconel 718 Processed by Selective Laser Melting," J. Mater. Sci. Technol., **34**(10), pp. 1799–1804.

[33]   Thijs, L., Kempen, K., Kruth, J.-P., and Van Humbeeck, J., 2013, "Fine-Structured Aluminium Products with Controllable Texture by Selective Laser Melting of Pre-Alloyed AlSi10Mg Powder," Acta Mater., **61**(5), pp. 1809–1819.

[34]   Scipioni Bertoli, U., MacDonald, B. E., and Schoenung, J. M., 2019, "Stability of Cellular Microstructure in Laser Powder Bed Fusion of 316L Stainless Steel," Mater. Sci. Eng. A, **739**, pp. 109–117.

[35]   Cheng, M., Xiao, X., Luo, G., and Song, L., 2021, "Integrated Control of Molten Pool Morphology and Solidification Texture by Adjusting Pulse Duration in Laser Additive Manufacturing of Inconel 718," Opt. Laser Technol., **142**.

[36]   Hagihara, K., Ishimoto, T., Suzuki, M., Ozasa, R., Matsugaki, A., Wang, P., and Nakano, T., 2021, "Factor Which Governs the Feature of Texture Developed during Additive Manufacturing; Clarified from the Study on Hexagonal C40-NbSi2," Scr. Mater., **203**.

[37]   Zhao, S., Shen, X., Yang, J., Teng, W., and Wang, Y., 2018, "Densification Behavior and Mechanical Properties of Nanocrystalline TiC Reinforced 316L Stainless Steel Composite Parts Fabricated by Selective Laser Melting," Opt. Laser Technol., **103**, pp. 239–250.

[38]   Langi, E., Zhao, L. G., Jamshidi, P., Attallah, M. M., Silberschmidt, V. V., Willcock, H., and Vogt, F., 2021, "Microstructural and Mechanical Characterization of Thin-Walled Tube Manufactured with Selective Laser Melting for Stent Application," J. Mater. Eng. Perform., **30**(1), pp. 696–710.

[39]   Murkute, P., Pasebani, S., and Isgor, O. B., 2019, "Production of Corrosion-Resistant 316L Stainless Steel Clads on Carbon Steel Using Powder Bed Fusion-Selective Laser Melting," J. Mater. Process. Technol., **273**.

[40]   Hong, Y., Zhou, C., Zheng, Y., Zhang, L., and Zheng, J., 2021, "The Room Temperature Creep of Selective Laser Melted 316L Stainless Steel Investigated by Nanoindentation," J. Mater. Eng. Perform., **30**(9), pp. 6502–6510.

[41]   Tjong, S. C., 2007, "Novel Nanoparticle-Reinforced Metal Matrix Composites with Enhanced Mechanical Properties," Adv. Eng. Mater., **9**(8), pp. 639–652.

[42]   Mussatto, A., Groarke, R., Vijayaraghavan, R. K., Obeidi, M. A., McNally, P. J., Nicolosi, V., Delaure, Y., and Brabazon, D., 2022, "Laser-Powder Bed Fusion of Silicon Carbide Reinforced 316L Stainless Steel Using a Sinusoidal Laser Scanning Strategy," J. Mater. Res. Technol., **18**, pp. 2672–2698.

[43]   Qiu, C., Kindi, M. A., Aladawi, A. S., and Hatmi, I. A., 2018, "A Comprehensive Study on Microstructure and Tensile Behaviour of a Selectively Laser Melted Stainless Steel," Sci. Rep., **8**(1).

[44]   Yin, H., Song, M., Deng, P., Li, L., Prorok, B. C., and Lou, X., 2021, "Thermal Stability and Microstructural Evolution of Additively Manufactured 316L Stainless Steel by Laser Powder Bed Fusion at 500–800 °C," Addit. Manuf., **41**.

[45]   Lippold, J. C., 2015, *Welding Metallurgy and Weldability*, John Wiley & Sons, New Jersey.

[46] Upadhyay, M. V., Slama, M. B. H., Gaudez, S., Mohanan, N., Yedra, L., Hallais, S., Héripré, E., and Tanguy, A., 2021, "Non-Oxide Precipitates in Additively Manufactured Austenitic Stainless Steel," Sci. Rep., **11**(1).

[47] Folkhard, E., 2012, *Welding Metallurgy of Stainless Steels*, Springer Science & Business Media, Vienna, Austria.

[48] Dutta Majumdar, J., Kumar, A., and Li, L., 2009, "Direct Laser Cladding of SiC Dispersed AISI 316L Stainless Steel," Tribol. Int., **42**(5), pp. 750–753.

[49] Dilip, J. J. S., Zhang, S., Teng, C., Zeng, K., Robinson, C., Pal, D., and Stucker, B., 2017, "Influence of Processing Parameters on the Evolution of Melt Pool, Porosity, and Microstructures in Ti-6Al-4V Alloy Parts Fabricated by Selective Laser Melting," Prog. Addit. Manuf., **2**(3), pp. 157–167.

[50] Wakai, Y., Ogura, T., Nakano, S., Sato, N., Kajino, S., and Suzuki, S., 2020, "Melting Behavior in Laser Powder Bed Fusion Revealed by in Situ X-Ray and Thermal Imaging," Int. J. Adv. Manuf. Technol., **110**(3), pp. 1047–1059.

[51] Fan, Z., Lu, M., and Huang, H., 2018, "Selective Laser Melting of Alumina: A Single Track Study," Ceram. Int., **44**(8), pp. 9484–9493.

[52] Fischer, R., Ting, A., DiComo, G., Prosser, J., Peñano, J., Hafizi, B., and Sprangle, P., 2009, "Absorption and Scattering of 1.06 Um Laser Radiation from Oceanic Aerosols," Appl. Opt., **48**(36), pp. 6990–6999.

[53] Semak, V. V., Gerakis, A., and Shneider, M. N., 2019, "Measurement of Temperature Dependent Absorption Coefficient of Water at 1064nm Wavelength," AIP Adv., **9**(8).

[54] Putri, K. Y., Yulianto, N., and Herbani, Y., 2017, "Study on Acoustic Detections of Nd:YAG Laser Induced Breakdown at Different Wavelengths," J. Phys. Conf. Ser., **817**.

[55] Ho, J. R., Grigoropoulos, C. P., and Humphrey, J. a. C., 1995, "Computational Study of Heat Transfer and Gas Dynamics in the Pulsed Laser Evaporation of Metals," J. Appl. Phys., **78**(7), pp. 4696–4709.

[56] Matthews, M. J., Guss, G., Khairallah, S. A., Rubenchik, A. M., Depond, P. J., and King, W. E., 2016, "Denudation of Metal Powder Layers in Laser Powder Bed Fusion Processes," Acta Mater., **114**, pp. 33–42.

[57] Sun, Z., Tan, X., Tor, S. B., and Chua, C. K., 2018, "Simultaneously Enhanced Strength and Ductility for 3D-Printed Stainless Steel 316L by Selective Laser Melting," NPG Asia Mater., **10**(4), pp. 127–136.

[58] Zhao, C., Fezzaa, K., Cunningham, R. W., Wen, H., De Carlo, F., Chen, L., Rollett, A. D., and Sun, T., 2017, "Real-Time Monitoring of Laser Powder Bed Fusion Process Using High-Speed X-Ray Imaging and Diffraction," Sci. Rep., **7**(1), p. 3602.

[59] Liu, S. Y., Li, H. Q., Qin, C. X., Zong, R., and Fang, X. Y., 2020, "The Effect of Energy Density on Texture and Mechanical Anisotropy in Selective Laser Melted Inconel 718," Mater. Des., **191**.

[60] Obeidi, M. A., Conway, A., Mussatto, A., Dogu, M. N., Sreenilayam, S. P., Ayub, H., Ahad, I. U., and Brabazon, D., 2022, "Effects of Powder Compression and Laser Re-Melting on the Microstructure and Mechanical Properties of Additively Manufactured Parts in Laser-Powder Bed Fusion," Results Mater., **13**(100264).

[61] Weingarten, C., Buchbinder, D., Pirch, N., Meiners, W., Wissenbach, K., and Poprawe, R., 2015, "Formation and Reduction of Hydrogen Porosity during Selective Laser Melting of AlSi10Mg," J. Mater. Process. Technol., **221**, pp. 112–120.

[62] Haiyan, G., Xiaoming, R., Jianguo, S., Wang, C., Baode, S., Qing, Z., Jun, W., and Zili, L., 2012, *Fe-X-C Crystal Grain Refiner and Preparation Method Thereof,*

Patent Number CN102277523B, Shanghai Jiaotong University, Baoshan Iron and Steel Co Ltd, China.

[63]   Kusoglu, I. M., Gökce, B., and Barcikowski, S., 2020, "Use of (Nano-)Additives in Laser Powder Bed Fusion of Al Powder Feedstocks: Research Directions within the Last Decade," Procedia CIRP, **94**, pp. 11–16.

[64]   Fan, Z., Gao, F., Wang, Y., Men, H., and Zhou, L., 2022, "Effect of Solutes on Grain Refinement," Prog. Mater. Sci., **123**(A Festschrift in Honor of Brian Cantor).

[65]   Matlock, D. K., and Speer, J. G., 2010, "Processing Opportunities for New Advanced High-Strength Sheet Steels," Mater. Manuf. Process., **25**(1–3), pp. 7–13.

[66]   Watari, T., Nansai, K., and Nakajima, K., 2021, "Major Metals Demand, Supply, and Environmental Impacts to 2100: A Critical Review," Resour. Conserv. Recycl., **164**.

[67]   Salvo, C., Mangalaraja, R. V., Udayabashkar, R., Lopez, M., and Aguilar, C., 2019, "Enhanced Mechanical and Electrical Properties of Novel Graphene Reinforced Copper Matrix Composites," J. Alloys Compd., **777**, pp. 309–316.

[68]   Gao, S., Nan, Z., Li, Y., Zhao, N., Liu, Q., Xu, G., Cheng, X., and Yang, J., 2020, "Copper Matrix Thermal Conductive Composites with Low Thermal Expansion for Electronic Packaging," Ceram. Int., **46**(11, Part A), pp. 18019–18025.

[69]   Sillani, F., de Gasparo, F., Schmid, M., and Wegener, K., 2021, "Influence of Packing Density and Fillers on Thermal Conductivity of Polymer Powders for Additive Manufacturing," Int. J. Adv. Manuf. Technol., **117**(7), pp. 2049–2058.

[70]   Ummartyotin, S., Bunnak, N., Juntaro, J., Sain, M., and Manuspiya, H., 2012, "Synthesis of Colloidal Silver Nanoparticles for Printed Electronics," Comptes Rendus Chim., **15**(6), pp. 539–544.

[71]   Luo, D., Xiao, Y., Hardwick, L., Snell, R., Way, M., Sanuy Morell, X., Livera, F., Ludford, N., Panwisawas, C., Dong, H., and Goodall, R., 2021, "High Entropy Alloys as Filler Metals for Joining," Entropy, **23**(1), p. 78.

[72]   Chuang, T. H., Tsao, L. C., Tsai, T. C., Yeh, M. S., and Wu, C. S., 2000, "Development of a Low-Melting-Point Filler Metal for Brazing Aluminum Alloys," Metall. Mater. Trans. A, **31**(9), pp. 2239–2245.

[73]   Muhrat, A., Puga, H., and Barbosa, J., 2018, "Low-Temperature Brazing of Titanium Using Al-Based Filler Alloys," Adv. Mater. Sci. Eng., **2018**.

[74]   Way, M., Willingham, J., and Goodall, R., 2020, "Brazing Filler Metals," Int. Mater. Rev., **65**(5), pp. 257–285.

[75]   Zavala-Arredondo, M., Boone, N., Willmott, J., Childs, D. T. D., Ivanov, P., Groom, K. M., and Mumtaz, K., 2017, "Laser Diode Area Melting for High Speed Additive Manufacturing of Metallic Components," Mater. Des., **117**, pp. 305–315.

[76]   Li, N., Liu, W., Wang, Y., Zhao, Z., Yan, T., Zhang, G., and Xiong, H., 2021, "Laser Additive Manufacturing on Metal Matrix Composites: A Review," Chin. J. Mech. Eng., **34**(1), p. 38.

[77]   Jadhav, S. D., Dhekne, P. P., Brodu, E., Van Hooreweder, B., Dadbakhsh, S., Kruth, J.-P., Van Humbeeck, J., and Vanmeensel, K., 2021, "Laser Powder Bed Fusion Additive Manufacturing of Highly Conductive Parts Made of Optically Absorptive Carburized CuCr1 Powder," Mater. Des., **198**.

[78]   Gu, D., Yang, Y., Xi, L., Yang, J., and Xia, M., 2019, "Laser Absorption Behavior of Randomly Packed Powder-Bed during Selective Laser Melting of SiC and TiB2 Reinforced Al Matrix Composites," Opt. Laser Technol., **119**.

[79]   Constantin, L., Kraiem, N., Wu, Z., Cui, B., Battaglia, J.-L., Garnier, C., Silvain, J.-F., and Lu, Y. F., 2021, "Manufacturing of Complex Diamond-Based Composite Structures via Laser Powder-Bed Fusion," Addit. Manuf., **40**.

[80]   Lahoz, R., Natividad, E., Mayoral, Á., Rentenberger, C., Díaz-Fernández, D., Félix, E. J., Soriano, L., Kautek, W., and Bomati-Miguel, O., 2020, "Pursuit of Optimal Synthetic Conditions for Obtaining Colloidal Zero-Valent Iron Nanoparticles by Scanning Pulsed Laser Ablation in Liquids," J. Ind. Eng. Chem., **81**, pp. 340–351.

[81]   Jiménez, A., Bidare, P., Hassanin, H., Tarlochan, F., Dimov, S., and Essa, K., 2021, "Powder-Based Laser Hybrid Additive Manufacturing of Metals: A Review," Int. J. Adv. Manuf. Technol., **114**(1), pp. 63–96.

[82]   Walachowicz, F., Bernsdorf, I., Papenfuss, U., Zeller, C., Graichen, A., Navrotsky, V., Rajvanshi, N., and Kiener, C., 2017, "Comparative Energy, Resource and Recycling Lifecycle Analysis of the Industrial Repair Process of Gas Turbine Burners Using Conventional Machining and Additive Manufacturing," J. Ind. Ecol., **21**(S1), pp. S203–S215.

[83]   Bidare, P., Jiménez, A., Hassanin, H., and Essa, K., 2021, "Porosity, Cracks, and Mechanical Properties of Additively Manufactured Tooling Alloys: A Review," Adv. Manuf.

[84]   Rahito, Wahab, D. A., and Azman, A. H., 2019, "Additive Manufacturing for Repair and Restoration in Remanufacturing: An Overview from Object Design and Systems Perspectives," Processes, **7**(11), p. 802.

[85]   Aswal, V. K., Jain, J. K., and Sonia, P., 2021, "Review on the Behavior of Various Parameters on Heat Distribution in the SAW Process," Mater. Today Proc., **47**, pp. 6734–6739.

[86]   Baghel, A., Sharma, C., Rathee, S., and Srivastava, M., 2021, "Influence of Activated Flux on Micro-Structural and Mechanical Properties of AISI 1018 during MIG Welding," Mater. Today Proc., **47**, pp. 6947–6952.